



# $\alpha$ -Fe<sub>2</sub>O<sub>3</sub>@carbon core–shell nanostructure for luminescent upconversion and photocatalytic degradation of methyl orange

Gnanasekaran Munusamy<sup>1</sup> · Rajaboopathi Mani<sup>2</sup> ·  
Krishnakumar Varadharajan<sup>1</sup> · Surumbarkuzhali Narasimhan<sup>3</sup> ·  
Chitharaj Munusamy<sup>1</sup> · Boopathy Chandrasekaran<sup>1</sup>

Received: 15 May 2019 / Accepted: 16 September 2019 / Published online: 24 September 2019  
© Springer Nature B.V. 2019

## Abstract

The unique characteristics of metal–organic frameworks such as structural tunability, high surface area, low density, and tailored porosity have made this material suitable for different applications, compared to mineralized carbons. To improve the photocatalytic activity of  $\alpha$ -Fe<sub>2</sub>O<sub>3</sub>, a shell of carbon with different concentrations on the core of  $\alpha$ -Fe<sub>2</sub>O<sub>3</sub> was prepared via hydrothermal method. The optical property, crystal phase, and morphology of the synthesized materials were characterized by X-ray diffraction, X-ray photoelectron spectroscopy, energy-dispersive X-ray spectrometer, scanning electron microscopy, and high-resolution transmission electron microscopy (HR-TEM). The HR-TEM shows a single-sphere core–shell structure of  $\alpha$ -Fe<sub>2</sub>O<sub>3</sub> at higher concentration of carbon ( $\alpha$ FC3), which showed a maximum degradation of pollutant about 85% in 2 h and 40 min. It is reasoned that the major dominants O<sub>2</sub><sup>-</sup> and h<sup>+</sup> enhance the degradation. The Fe<sup>3+</sup> ions strongly promote the upconversion emission observed at excitation of 620 nm. Photocurrent and Mott–Schottky revealed that the  $\alpha$ FC3 core–shell sample shows that the  $-0.157$  flat-band potential ( $V_{fb}$ ) increased the carrier density in the near-surface region accelerating the redox performances. In short, the excellent visible light degradation ability of  $\alpha$ FC3 against the methyl orange and high upconversion efficiency were observed in  $\alpha$ -Fe<sub>2</sub>O<sub>3</sub>@carbon core–shell nanostructure.

✉ Gnanasekaran Munusamy  
gnanasekaran2590@gmail.com

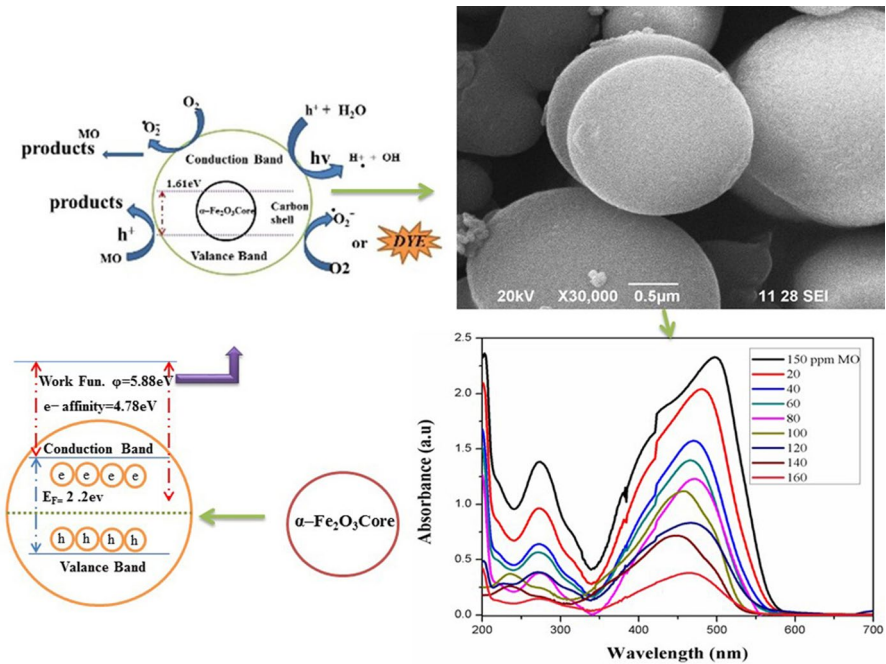
✉ Krishnakumar Varadharajan  
vkrishna\_kumar@yahoo.com

<sup>1</sup> School of Physical Sciences, Periyar University, Salem, Tamil Nadu 636011, India

<sup>2</sup> Centre for Research and Development, PRIST Deemed to be University, Thanjavur, Tamil Nadu 613403, India

<sup>3</sup> Department of Physics, Government Arts College, Salem, Tamilnadu 636007, India

## Graphic abstract



**Keywords**  $\alpha\text{-Fe}_2\text{O}_3$  · Core-shell · Photoluminescence · Methylene orange · Photocatalytic activity

## Introduction

Advanced oxidation processes (AOPs) are potential strategies for the treatment of industrial wastewater containing non-biodegradable organic pollutants which have been attracted much for the past decades. Creation of free hydroxyl radical ( $\cdot\text{OH}$ ) degrades most organic pollutants quickly and non-selectively. Methylene orange (MO) is well-known representative dyes which has been widely used in textile, printing, and research laboratories [1–7]. The  $\alpha\text{-Fe}_2\text{O}_3$  possess excellent band gap (2.2 eV) which leads to better photocatalytic degradation [8, 9]. Because of band structure it produces hydroxyl radicals ( $\cdot\text{OH}$ ) and superoxide radicals ( $\text{O}_2^-$ ) through light-driven chemical reactions. Core-shell materials have been attracted for the degradation of dyes due to their superior optical and electrical properties, which govern physical dimension, structure, size, and shape compared to nanocomposite materials. The upconversion-based UV-visible photocatalyst has two major challenges to achieve better photocatalytic efficiency. (1) How to efficiently utilize the upconversion energy transferred from the materials? (2) How

to suppress the photogenerated e<sup>-</sup> and h<sup>+</sup> recombination after excited by upconversion energy? The former can be realized by constructing core–shell structure, thereby protecting the upconversion from surface quenching and increasing the energy transfer efficiency [10–12]. The local magnetic moment and strong local lattice distortion in the  $\alpha$ FC3 sample easily generate e<sup>-</sup> and h<sup>+</sup> after excitation. It rectifies the latter challenge. The photon upconversion (UC) is a nonlinear optical process in which two or more low-energy photons, typically in the near-infrared (NIR) range, are sequentially absorbed and converted into emitted photons of higher energy in the UV–visible range [13–15]. Recently, the hematite ( $\alpha$ -Fe<sub>2</sub>O<sub>3</sub>) materials' anisotropy properties absorbed in the microstructure exhibited excellent photocatalytic activity [16]. The surface-controlled of  $\alpha$ -Fe<sub>2</sub>O<sub>3</sub> has been reported elsewhere [17, 18]. The  $\alpha$ -Fe<sub>2</sub>O<sub>3</sub> and carbon surface-controlled core–shell structure shown excellent photocatalytic activity [19, 20]. Hereby, we reported  $\alpha$ -Fe<sub>2</sub>O<sub>3</sub>@carbon ( $\alpha$ -FC3) core–shell spherical materials to improve the upconversion luminescence and ensure high photocatalytic stability against redox of the core–shell systems [21, 22]. In our synthesis, we obtained an eccentric compact sphere-shaped  $\alpha$ -Fe<sub>2</sub>O<sub>3</sub> surrounded by carbon without any metallic substrates [23]. Recently, an ultrasound-assisted synthesized route provided a nano-/microstructure at 20–100 kHz [5, 24, 25]. A hematite ( $\alpha$ -Fe<sub>2</sub>O<sub>3</sub>) is one of the most stable iron oxides with n-type semiconducting properties. It is used in various applications such as catalysts, pigments, water treatment, magnetic materials, sensors, and lithium-ion batteries because of its low cost, simple production, environment friendly, and excellent chemical stability. The bandgap of  $\alpha$ -Fe<sub>2</sub>O<sub>3</sub> is 2.2 eV which absorbs visible light, thereby becoming a promising photocatalyst [21, 22, 26]. This work discusses visible light-driven photocatalytic efficiency and upconversion of Fe<sub>2</sub>O<sub>3</sub>@carbon, and as a proof of idea, this work gives new bits of knowledge of the upconversion depend end approach to UV–Vis–NIR-driven photocatalysis by consolidation of core–shell materials.

## Experimental sections

### Materials and methods

All the chemicals were of analytical grade purchased from Sigma-Aldrich and used without further purification.

### Synthesis of $\alpha$ -Fe<sub>2</sub>O<sub>3</sub> nanoparticles

A solution of 0.5 M of iron (III) chloride ((FeCl<sub>3</sub>, 4.8 g) at 60 ml of deionized water and 0.5 M of urea ((NH<sub>2</sub>CONH<sub>2</sub>, 0.6 g) at 20 ml ethanedial (C<sub>2</sub>H<sub>2</sub>O<sub>2</sub>) was prepared separately. The latter solution was dropwise added into the former solution and vigorously mixed for 30 min. The obtained suspension was transferred into 100-ml Teflon-lined autoclave and placed in an oven at 180 °C for 12 h. The sample was allowed naturally to reach the room temperature, and then the final

products were collected and centrifuged by three times with deionized water and ethanol ( $C_2H_5OH$ ) subsequently. The  $\alpha\text{-Fe}_2O_3$  samples were dried in an oven at  $80\text{ }^\circ\text{C}$  for 12 h.

### Synthesis of $\alpha\text{FC1}$ , $\alpha\text{FC2}$ , and $\alpha\text{FC3}$ sphere particles

In a typical procedure, 0.3 M glucose ( $C_6H_{12}O_6$ , 0.16 g) was dissolved in 60 ml of distilled water. A 500 mg of  $\alpha\text{-Fe}_2O_3$  prepared nanoparticle was added into the above solution and dispersed well using low-frequency sonophoresis (LFS). This LFS PA124 process (Precision Acoustics Ltd, calibration range: 10 kHz–20 MHz, sensor diameter: 25 mm) exponentially increases the absorption of carbon. The local densification in the mixed solution due to superfluous molecules induces nucleation on the surrounding core materials by LFS process with 20 kHz for 1 h. The solution was transferred into 100-ml Teflon-lined autoclave maintained at  $160\text{ }^\circ\text{C}$  for 24 h. It was naturally cooled down to room temperature to obtain the final products. It was centrifuged and washed with ethanol and distilled water. The samples were dried at  $80\text{ }^\circ\text{C}$  for 12 h and obtained the spherical particle of  $\alpha\text{-Fe}_2O_3@C_{3\%}$  ( $\alpha\text{FC1}$ ). The other samples  $\alpha\text{-Fe}_2O_3@C_{6\%}$  ( $\alpha\text{FC2}$ ) and  $\alpha\text{-Fe}_2O_3@C_{9\%}$  ( $\alpha\text{FC3}$ ) were prepared by varying carbon concentration by maintaining the  $\alpha\text{-Fe}_2O_3$  with 500 mg. The obtained samples were stored in a desiccator and used for further characterization.

### Characterization

The powder X-ray diffraction (XRD) patterns of samples were obtained from the Rigaku X-ray diffractometer using  $\text{Cu-K}\alpha$  radiation  $k=1.54\text{ \AA}$  in the  $2\theta$  range of  $20^\circ\text{--}80^\circ$  at room temperature with a scanning rate of  $0.06^\circ/\text{s}$ . The surface elemental analysis was conducted on X-ray photoelectron spectroscopy (XPS) (SPECS GmbH spectrometer with PHOIBOS 100MCD energy analyzer) depth profiling facility. The Fourier transform infrared (FTIR) spectra were recorded using Bruker Tensor 27 spectrophotometer with resolution of  $2\text{ cm}^{-1}$  in the range of  $4000\text{--}400\text{ cm}^{-1}$  at regular KBr phase. The high-resolution transmission electron microscopy (HR-TEM) images were recorded by JEOL JEM-2010 at accelerating voltage of 200 kV. The Hitachi S-4800 scanning electron microscope (SEM) was used to find out the surface morphology at 20 kV. The presence of surface morphology and elemental compositions presented in the samples was identified by energy-dispersive X-ray spectrometer (EDS) using Oxford INCA II energy solid-state detector. The UV–Vis diffuse reflectance spectrometer (UV–Vis DRS, Ocean Optics PX-2) equipped with a pulsed xenon light source was used over a range of 200–800 nm. The photoluminescence (PL) spectrum was recorded by FL-7000 spectrophotometer using room temperature emission and excitation spectra for finely ground solid powder with a scanning rate of 1200 nm/min.

## Photocurrent measurement

The transient photocurrent spectrum was recorded on SP-150 Bio-Logic Science Instruments, France. It was three-electrode systems of counter electrode Pt, Ag/AgCl and reference electrode in saturated KCl solution. The photocatalyst sample was coated on a fluorine-doped tin oxide (FTO) substrate to use as a working electrode. 20 mg of the photocatalyst samples, 500  $\mu$ l ethanol and 100  $\mu$ l Nafion solution were dispersed by 1 h ultrasonication. It was spin-coated on pre-cleaned FTO glass substrate at 2000 rpm for 5 min. The obtained working electrodes were dried at room temperature, and active surface area was fixed as ca. 1 cm<sup>2</sup> using Teflon tape. A 150-W xenon lamp was used as a light source, and 0.5 M NaCl aqueous solution was served as the electrolyte for photocurrent measurement. N<sub>2</sub> gas was continuously bubbled in solution before and during the experiment to remove any dissolved O<sub>2</sub> and therefore suppress the reduction of O<sub>2</sub> at the counter electrode. The transient photocurrent response of the prepared electrodes was recorded under the light on-off condition.

## Photocatalytic activity of $\alpha$ FC1, $\alpha$ FC2, and $\alpha$ FC3 sphere particles

The photocatalytic activity of all the samples was performed by degradation of MO dyes under visible light irradiation. For assessing degradation ability, 100 mg of sample was dispersed in MO aqueous solution, which had prepared previously in water with MO concentration of 150 ppm. The photocatalytic solution was adjusted to pH 5 using NH<sub>4</sub>OH. The solution was stirred for 20 min to ensure the adsorption-desorption equilibrium between the photocatalyst and the target pollutants. Then the solution was irradiated using 500-W halogen lamp placed at 15 cm away from the solution surface, and the reactor temperature was maintained at 25 °C using water circulated-jacketed reactor. The solution was withdrawn at every 20-min intervals using pipette and centrifuged to remove the possible products at 800 rpm. The solution was transferred into 12  $\times$  5 cm quartz cuvette for absorption measurement. The ultraviolet-visible-near-infrared (UV-Vis-NIR) absorption measurement was performed on a PerkinElmer lambda 25 spectrophotometers to monitor the absorption spectra at every 20-min intervals during the MO concentration.

## Results and discussion

### X-ray diffraction

The crystalline structure of the samples was investigated by XRD, and the patterns are shown in Fig. 1a-c. All the samples are well crystallized, and patterns can be indexed to rhombohedral  $\alpha$ -Fe<sub>2</sub>O<sub>3</sub> (JCPDS No. 33-0664). The diffraction peaks with  $2\theta$  values of 24.14°, 33.10°, 35.61°, 40.85°, 49.44°, 56.16°, 57.2°, 62.55°, 64.10°, 78.67°, and 52.31° and the corresponding planes (012), (104), (110), (113), (024),

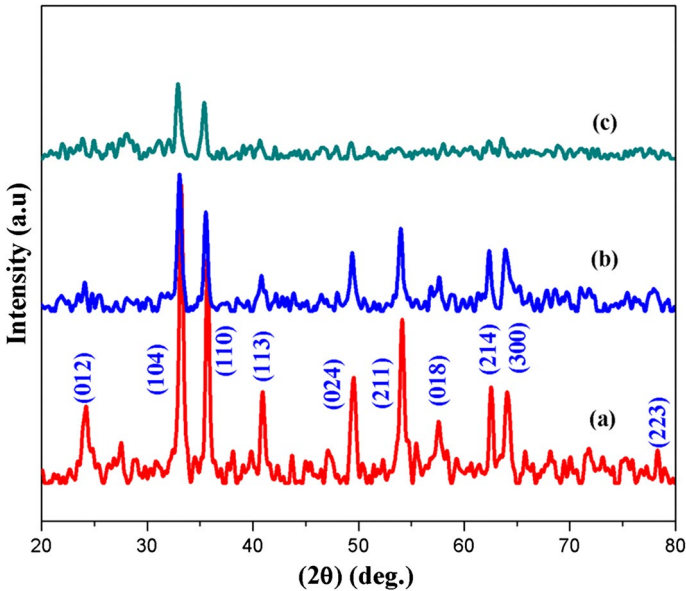


**Fig. 1** XRD patterns of **a**  $\alpha$ FC1, **b**  $\alpha$ FC2, and **c**  $\alpha$ FC3 sphere particles

(211), (018), (214), (300), and (223) are presented in Fig. 1a, respectively. No additional diffraction peaks appeared for carbon materials, and the diffraction intensities decreased were absorbed. The  $\alpha$ - $\text{Fe}_2\text{O}_3$  is an antiferromagnetic trigonal crystal system with space group of  $R\bar{3}c(D_{3d}^6)$  structure. Their lattice was built with a hexagonal array of oxygen with four of every six available octahedral sites occupied by Fe atoms. The  $\alpha$ - $\text{Fe}_2\text{O}_3$  lattice is built of Fe–Fe ions which lead to repulsion due to one shared face but no other oxygen atoms because their trigonal antiprism constructs very dense and high oxygen packing structure [27]. These results have appeared in the XRD pattern that diffraction intensity peaks decreased in  $\alpha$ FC2 and  $\alpha$ FC3 samples (Fig. 1b–c). These peaks become more intense as the loading amount of carbon increases indicating a decrease in the crystalline  $a$ ,  $c$  lattice parameter as shown in Table 1. The average crystallite size ( $D$ ) of the samples was calculated using Debye–Scherrer’s equation.

$$D = \frac{0.94\lambda}{\beta \cos \theta} \quad (1)$$

where  $\lambda$  is the wavelength of X-ray,  $\beta$  is the full-width at half-maximum corresponding to the intense peaks, and  $\theta$  is the diffraction angle. The average crystalline size reduction is due to single-sphere core–shell structure of  $\alpha$ FC3 sample. It is reasonably understood that in the  $\alpha$ FC3 core–shell sample, the carbon domain led the reconstruction of crystal phase or created new active interfaces at  $\alpha$ - $\text{Fe}_2\text{O}_3$  ions. The carbon is dominated in the lattice deformation compared to energy levels of  $\text{Fe}^{2+}$  and  $\text{Fe}^{3+}$  ions. In the  $\alpha$ - $\text{Fe}_2\text{O}_3$  crystal structure, rows of oxygen atoms are missing along  $c$ -axis which is easily occupied by carbon atoms. The influence of inclusion

**Table 1** The lattice constant and crystallite size of  $\alpha$ FC1,  $\alpha$ FC2, and  $\alpha$ FC3 samples

S. no	Samples	Miller indices (hkl)	Size of crystal (nm)	Average crystal size (nm)	Lattice parameter $a=b \neq c$ (Å)
1	$\alpha$ FC1	104	30.16	36.67	$a = 5.0739$
		110	43.18		$c = 13.735$
2	$\alpha$ FC2	104	27.36	29.95	$a = 4.9165$
		110	32.54		$c = 12.482$
3	$\alpha$ FC3	104	21.25	23.46	$a = 4.873$
		110	25.74		$c = 11.436$

is reflected in the lattice parameters as listed in Table 1. The similar lattice changes were observed elsewhere [28].

### X-ray photoelectron spectroscopy

The XPS survey spectrum of Fe, O, and C is shown in Fig. 2a–d. The XPS measurements were performed to determine the electronic states and surface chemical composition of  $\alpha$ -Fe<sub>2</sub>O<sub>3</sub>@carbon ( $\alpha$ FC3). As shown in Fig. 2c for the Fe 2*p* spectrum of Fe<sub>2</sub>O<sub>3</sub>, the binding energy for Fe 2*p*<sub>3/2</sub> is at ~708.95 eV and Fe 2*p*<sub>1/2</sub> is at ~723.05 eV [29]. The spin energy separation of  $\alpha$ -Fe<sub>2</sub>O<sub>3</sub> in 2*p*<sub>3/2</sub> and Fe 2*p*<sub>1/2</sub> indicates that the core–shell structure contains both Fe<sup>3+</sup> and Fe<sup>2+</sup> states. The survey scans of C 1*s* and O 1*s* are presented in Fig. 2b, d. The O 1*s* spectrum can be deconvoluted into two peaks, including a principal peak located at 530.85 eV and a shoulder peak at 531.3 eV. These peaks are attributed to oxygen species in the metal oxide (O<sup>2-</sup>) and the surface –OH group, respectively. In Fig. 2b, the C 1*s* spectrum can be deconvoluted into three peaks at 283.55 eV (C–C), 285.05 eV (C–O), and 287.55 eV (C=O) as reported elsewhere [30].

### FTIR analysis

The FTIR spectra of functional group presented in the as-synthesized sample are shown in Fig. 3. The broadband at 3440 cm<sup>-1</sup> is corresponding to O–H stretching vibration from glucose water content. The two vibrational frequencies observed at 556 cm<sup>-1</sup> and 467 cm<sup>-1</sup> related to Fe–O confirmed the hematite structure [31]. The characteristic peaks at 2923 and 2840 cm<sup>-1</sup> are attributed to CH<sub>3</sub> stretching vibration from glucose. The stretching vibrations presented at 1623 and 1710 cm<sup>-1</sup> are related to C=C and C=O cm<sup>-1</sup> [32]. The O–H bending vibration was presented at 1373 cm<sup>-1</sup>.

### Morphological characterization

The particle size and morphology of  $\alpha$ FC3 sample were identified by HR-TEM images as shown in Fig. 4a–d. In Fig. 4a, it is clear that the core–shell structure is prone to

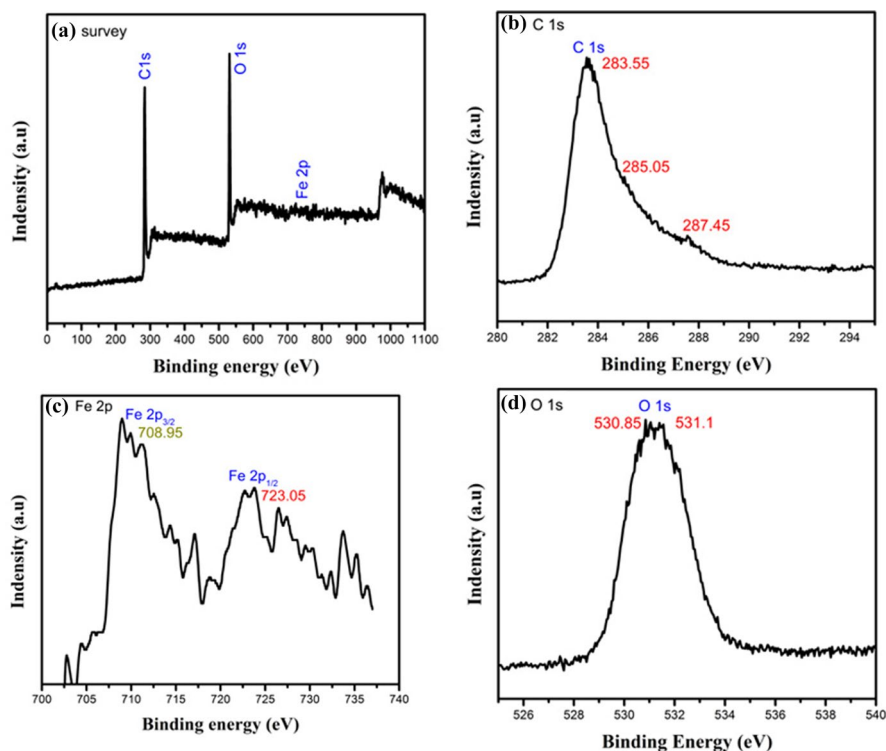


**Fig. 2** XPS spectra of  $\alpha$ FC3 sample **a** survey spectra, **b** C 1s, **c** Fe 2p, **d** O 1s core-shell material

form core ( $\alpha$ -Fe<sub>2</sub>O<sub>3</sub>) and shell (carbon) materials. The particle size of  $\alpha$ -Fe<sub>2</sub>O<sub>3</sub>@carbon is estimated to be 487.53 nm. The selected area electron diffraction (SAED) patterns of sample are presented in Fig. 4d. The interfacial angle of the diffraction is found to be 60°, and the corresponding fast fourier transform (FFT) pattern for the spot is (110), (−120), and (−210) [33]. The facet of the top surface of the particle is (001). It can be concluded from the images that the hematite nanocrystals are single crystalline in nature. The core-shell  $\alpha$ FC3 nanocrystals exhibit identical facet. The SEM images of  $\alpha$ FC1,  $\alpha$ FC2, and  $\alpha$ FC3 are presented in Fig. 5a–c. All the samples indicated the microsphere formation with carbon embedded by oxidizing agent [34]. A strong adsorption of carbon ions on the faces parallel to the *a*, *c*-axis of hexagonal  $\alpha$ -Fe<sub>2</sub>O<sub>3</sub> forms hexagonal  $\alpha$ FC1,  $\alpha$ FC2, and  $\alpha$ FC3. When increasing the carbon concentration, the high acidic condition in the  $\alpha$ FC2 and  $\alpha$ FC3 dissolves  $\alpha$ -Fe<sub>2</sub>O<sub>3</sub> along the *a*, *c*-axis to the inner part because the surfaces are adsorbing by Fe<sup>2+</sup>. The Fe<sup>2+</sup> ions are the key factor for the formation of core-shell  $\alpha$ FC3. In the  $\alpha$ FC1 and  $\alpha$ FC2, the Fe<sup>2+</sup> ions can also accelerate the formation of core-shell but not the determining factor of core-shell structure [35, 36]. The various concentrations of carbon lead to minor agglomeration on the surface forms core shell structure as presented in Fig. 5a. The  $\alpha$ FC2 shows hexagonal crystal structure as shown in Fig. 5b. The  $\alpha$ FC3



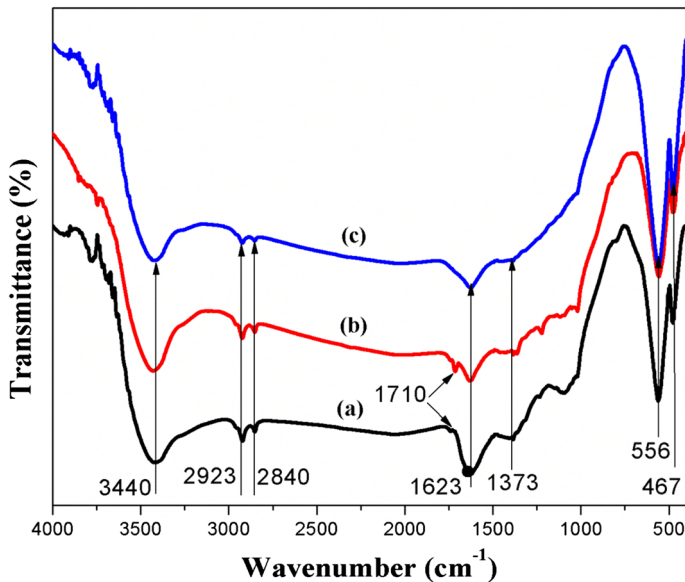


**Fig. 3** FTIR spectra of **a**  $\alpha$ FC1, **b**  $\alpha$ FC2, and **c**  $\alpha$ FC2 sphere particle

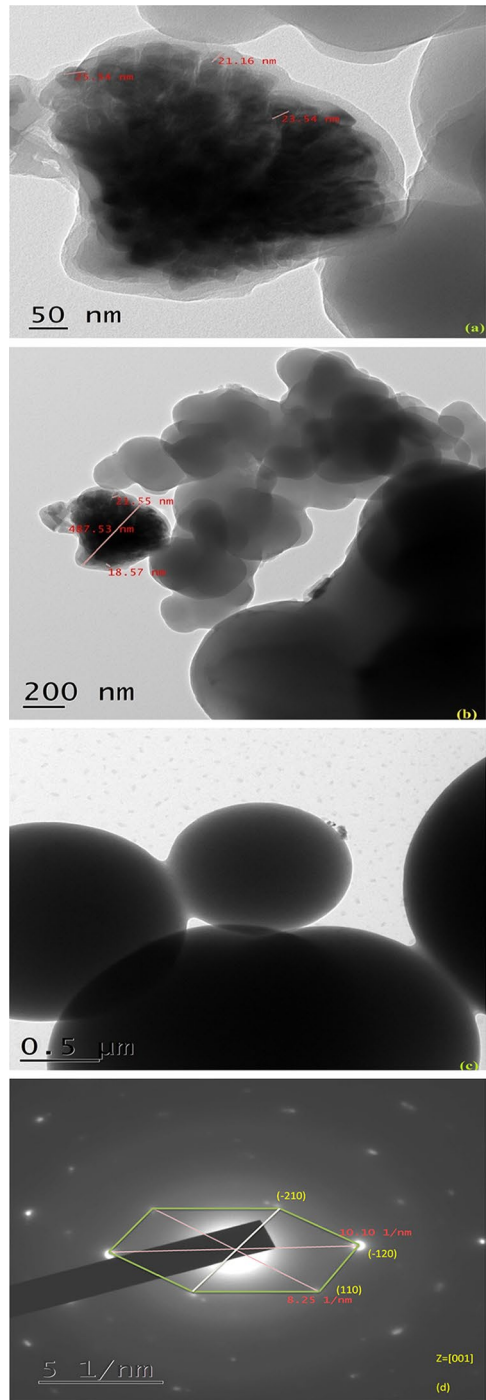
core–shell materials have been highly sphere-shaped (Fig. 5c). The primary  $\alpha$ -Fe<sub>2</sub>O<sub>3</sub> nanocrystals were capped by carbon domain.

The EDS quantitative spectra of  $\alpha$ FC1,  $\alpha$ FC2, and  $\alpha$ FC3 are presented in Fig. 6a–c. The EDS analysis shows that the presented chemicals are Fe, O, and C. The carbon peaks observed in the energy-dispersive X-ray spectrum are corresponding to  $\alpha$ FC1,  $\alpha$ FC2, and  $\alpha$ FC3 [37–39]. The high full-width at half-maximum of EDS peak in Fig. 6b, c is due to the high concentration of carbons. In the EDS spectra of Fig. 6a–c, two distinct peaks at 2.5 and 7.5 keV were due to Fe atoms. It is quantitatively dispersed from 0.5 and 6.5 keV of Fe atoms. The maximum carbon content would be obviously high at  $\alpha$ FC3 core–shell. The change in intensity reflects the changes in carbon concentrations.

### Investigation of optical property of $\alpha$ FC1, $\alpha$ FC2, and $\alpha$ FC3 sphere particles

The UV–DRS spectra of  $\alpha$ FC1,  $\alpha$ FC2, and  $\alpha$ FC3 are displayed in Fig. 7a. The strong absorption has been observed at 575 nm. The bandgap was increased considerably due to distinct energy of  $\alpha$ -Fe<sub>2</sub>O<sub>3</sub> by the ionic state of Fe<sup>2+</sup> and Fe<sup>3+</sup>. The Fe<sup>2+</sup> and Fe<sup>3+</sup> ions splitting encourage in  $\alpha$ -Fe<sub>2</sub>O<sub>3</sub>@carbon structure framework and surface site availability due to carbon contribution were reported [40]. The fastest recombination effect between the electron and hole of  $\alpha$ -Fe<sub>2</sub>O<sub>3</sub>@carbon materials from the valence and conduction band can be occurred via three different ways: (a) direct recombination through radiative and non-radiative; (b) trapping into intrinsic low-level electronic energy states through d–d coupling; and (c) trapping surface defect states. From the

**Fig. 4** HR-TEM images of  $\alpha$ FC3 core-shell sample. Different magnifications **a** 50 nm, **b** 200 nm, **c** 0.5  $\mu\text{m}$ , and **d** 5 1/nm



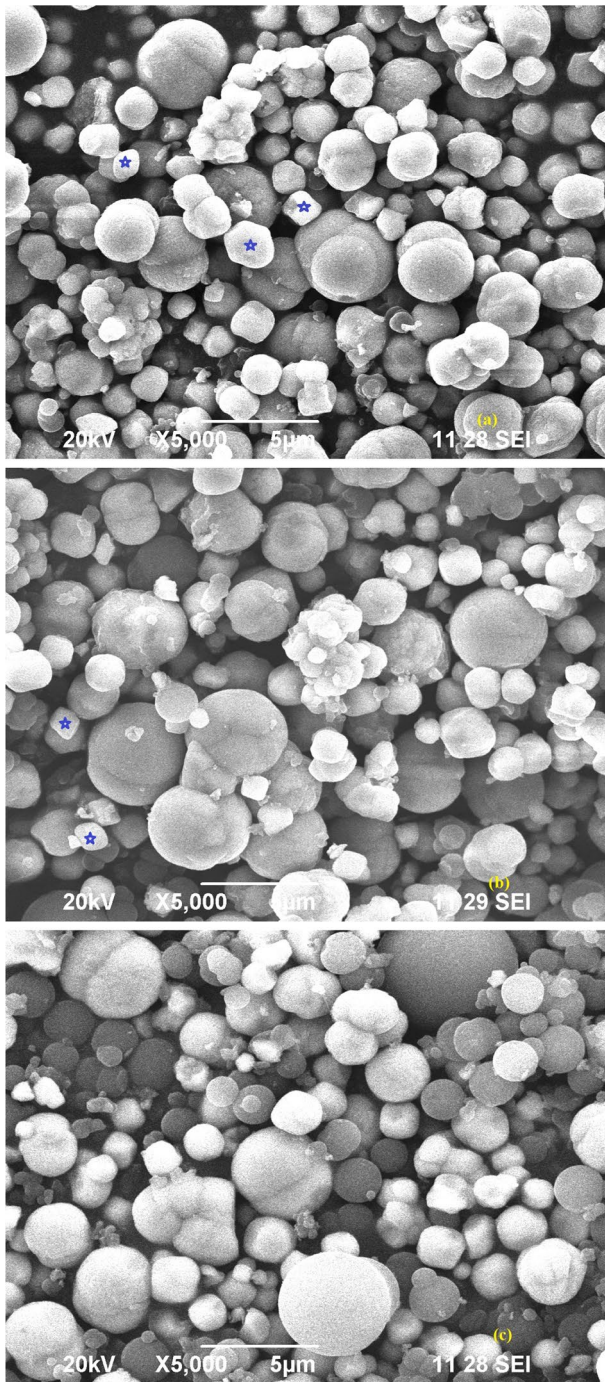
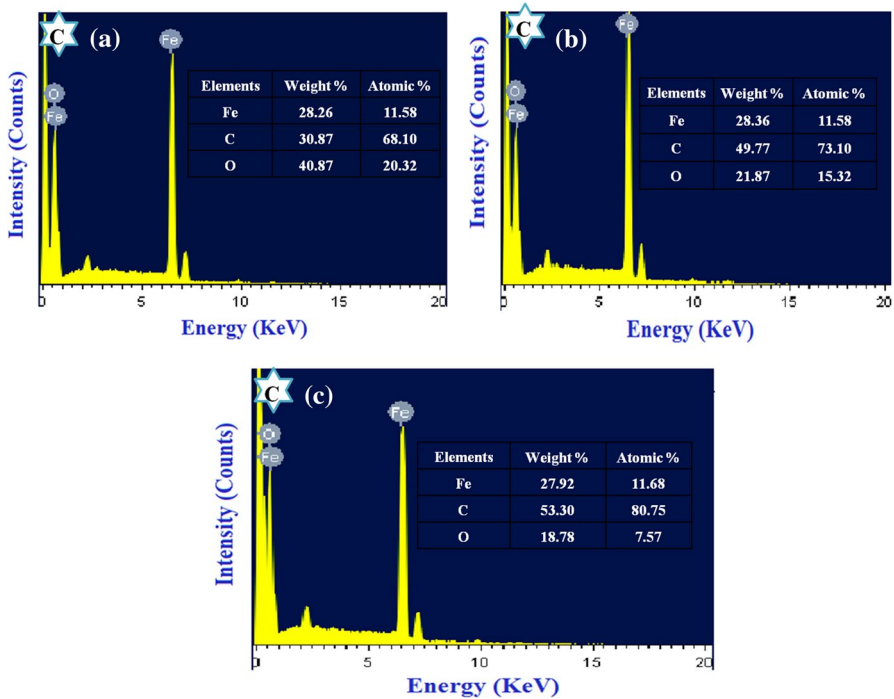


Fig. 5 SEM images of a  $\alpha$ FC1, b  $\alpha$ FC2, and c  $\alpha$ FC3 samples



**Fig. 6** EDS spectrum of **a**  $\alpha$ FC1, **b**  $\alpha$ FC2, and **c**  $\alpha$ FC3 sphere particles

above systematic process, nonlinear optical susceptibility in hematite has absorbed due to energy transition in  $\text{Fe}^{2+}$  and  $\text{Fe}^{3+}$  ions by recombination and trapping [41]. The tuned bandgap energies were calculated by Tauc plots as shown in Fig. 7b using the below equation [42].

$$(\alpha h\nu)^{1/n} = A(h\nu - E_g) \quad (2)$$

where  $h\nu$  is the incident photon energy,  $A$  is a constant, and  $n$  is the exponent. ' $n$ ' is determined by the type of electronic transition causing the absorption and can take the values  $1/2$  or  $2$  depending upon whether the transition is direct or indirect. Tauc plot is used to determine the direct bandgap values of  $\alpha$ FC1 = 1.56,  $\alpha$ FC2 = 1.5, and  $\alpha$ FC3 = 1.61 eV.

The photoluminescence emission spectra of  $\alpha$ FC1,  $\alpha$ FC2, and  $\alpha$ FC3 were determined for the excitation at 620 nm as shown in Fig. 8. The redshift occurs according to carbon concentration. The emission peaks were absorbed at  $\alpha$ FC1 = 550,  $\alpha$ FC2 = 541, and  $\alpha$ FC3 = 534 nm. The recombination and trapping from  $\text{Fe}^{2+}$  and  $\text{Fe}^{3+}$  ions and carbon electrons contribution cause for upconversion exhibited in  $\alpha$ - $\text{Fe}_2\text{O}_3$ @carbon materials via nonradioactive route. The nonradioactive route ultimately leads to an increase in thermal energy in the sample temperature. The typical spectrum shows spin-orbit interaction, where  $2p$  orbitals split  $2p_{1/2}$  and  $2p_{3/2}$  p-d coulomb and d-d exchanged interaction multiples [26, 43–45].

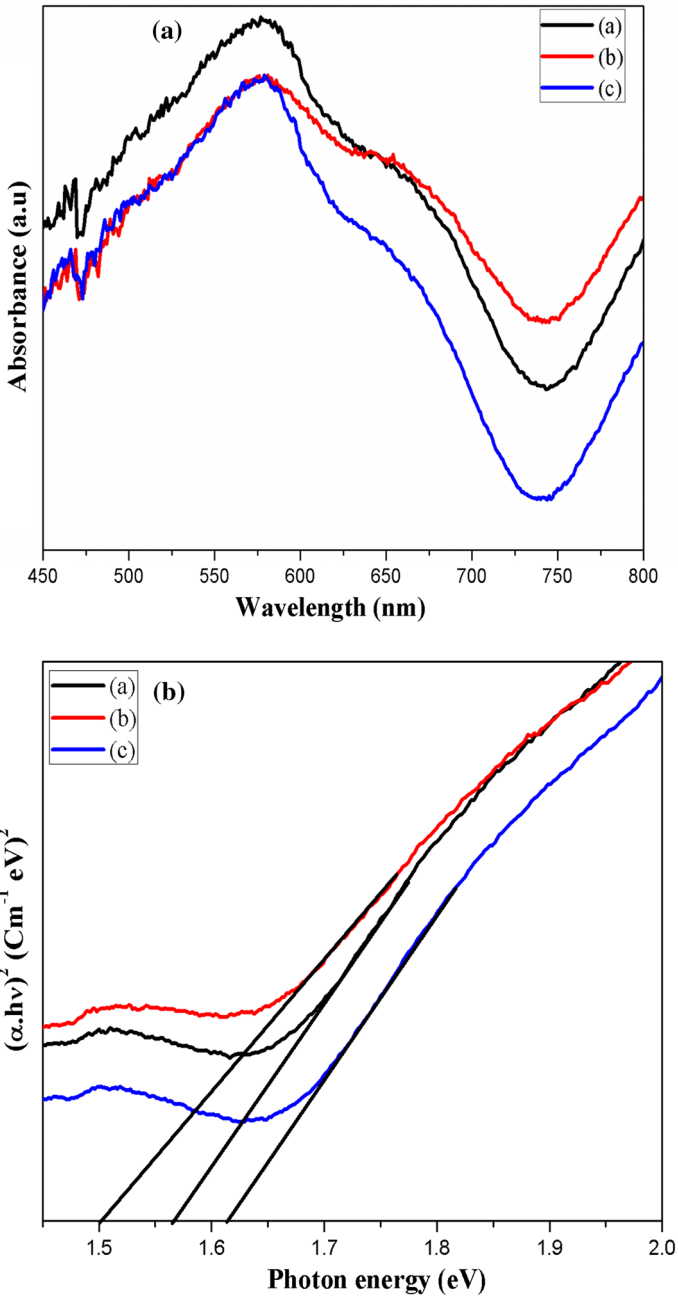


**Fig. 7** **a** UV-DRS spectra of  $\alpha$ FC1,  $\alpha$ FC2, and  $\alpha$ FC3 samples. **b** Tauc plot of  $\alpha$ FC1,  $\alpha$ FC2, and  $\alpha$ FC3 samples

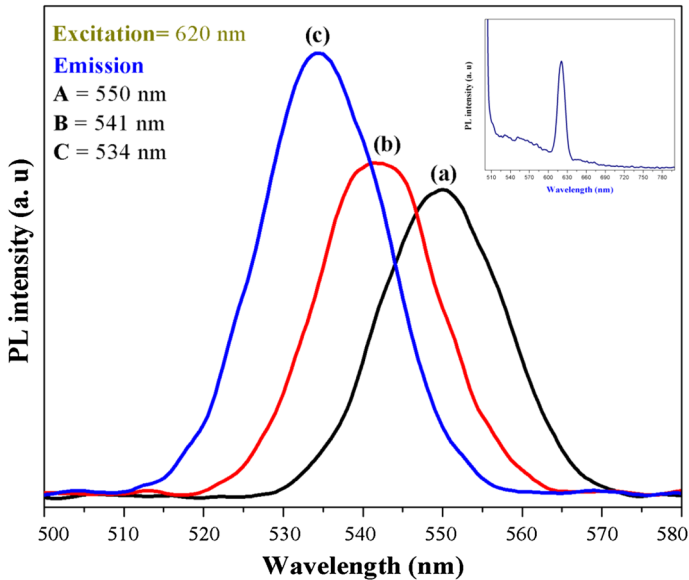


**Fig. 8** The upconversion fluorescence spectra of  $\alpha$ FC1,  $\alpha$ FC2, and  $\alpha$ FC3 samples

The presence of  $\text{Fe}^{3+}$  ions strongly depends on upconversion emissions because of quenching effect produced at 620-nm excitation. The quenching effect similarly can be eliminated with excitation at 850 nm [41, 46]. Hence, the  $\text{Fe}^{3+}$  ion does not suffer inner filter at 620 nm excitation, which is an added advantage of  $\alpha$ FC3 core-shell structure to activated upconversion. The  $\alpha$ FC3 core-shell can be attributed to the multiphoton active process similar to carbon and hematite which leads to long-lived excited d-d orbital's electron bound states. Finally, the hematite nanoparticles have a collapsed local magnetic moment and strong local lattice distortion in the antiferromagnetic background, which could generate an emission for photoexcitation [47, 48]. The  $\alpha$ FC1 and  $\alpha$ FC2 samples were compared to  $\alpha$ FC3 core-shell materials showing high PL emission. It shows the core-shell superior structure encourage after excitations and trapping magnetically coupled easily by antiferromagnetic nature.

### Photocurrent test

The photocurrent response of the  $\alpha$ FC1,  $\alpha$ FC2, and  $\alpha$ FC3 samples was recorded in several on-off cycles as shown in Fig. 9a. The photocurrent density was stable after 540 s on-off cycles. In contrast, all the samples surface-coated with high carbon content exhibited improved photocurrent performances. As shown in Fig. 2a-d of  $\alpha$ FC3 samples, the XPS signals with binding energy of the  $\text{Fe}^{3+}$  at 708.95 eV,  $\text{Fe}^{2+}$  at 723.05 eV, C 1s at 283.55–287.55 eV and O 1s between 530.85 and 531.3 eV, respectively, can be undoubtedly assigned to carbon. The decreased electron binding energy for  $\text{Fe}^{3+}$  and  $\text{Fe}^{2+}$  is unique for carbon in the metal-oxygen systems

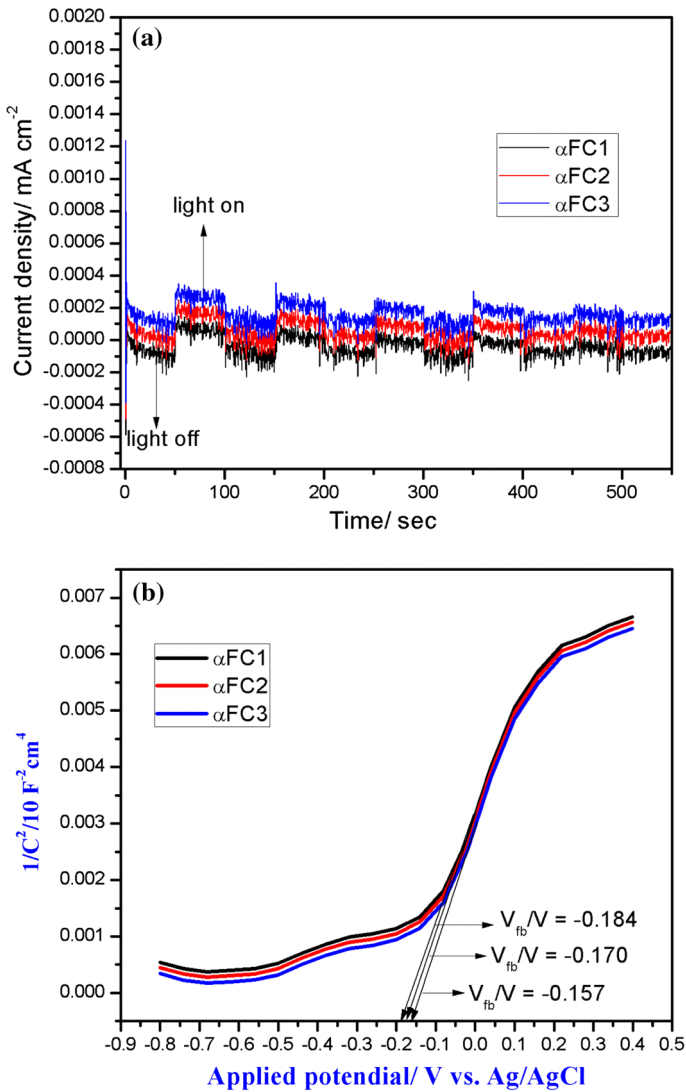


**Fig. 9** **a** Photocurrent of the  $\alpha\text{FC1}$ ,  $\alpha\text{FC2}$ , and  $\alpha\text{FC3}$  samples. **b** Mott–Schottky (M–S) plot of  $\alpha\text{FC1}$ ,  $\alpha\text{FC2}$ , and  $\alpha\text{FC3}$  samples

[49]. The high concentration of carbon is reason for the pronounced photocurrent improvement.

### Mott–Schottky analysis

In order to elucidate the electronic properties of  $\alpha\text{FC1}$ ,  $\alpha\text{FC2}$ , and  $\alpha\text{FC3}$  samples, the Mott–Schottky (M–S) plot was generated from TPC measurement (Fig. 9b). The smaller slope for the  $\alpha\text{FC3}$  sample reflects a higher electron donor density

[50]. The enhanced electrical conductivity can extend the lifetime of charge carriers. In addition,  $\alpha$ FC1 ( $-0.184$ ),  $\alpha$ FC2 ( $-0.17$ ), and  $\alpha$ FC3 ( $-0.157$ ) samples show that the flat-band potential ( $V_{fb}$ ) was cathodically shifted by 25 mV. This flat-band potential shift is probably due to the efficient electron–hole transport from  $\alpha$ FC3 sample, accelerating redox reaction.

### Photocatalytic evaluation

The degradation rate of  $\alpha$ FC3 against methyl orange (MO) in aqueous solution was tested by photocatalytic setup followed by absorption spectra. The degradation results are shown in Fig. 10a. The absorption peaks at 500–550 nm are corresponding to MO [7, 51]. The pseudo-first-order kinetics was calculated to determine the yields of chemical reaction by the following equation.

$$\ln(C_t/C_0) = -k_{app}t \quad (3)$$

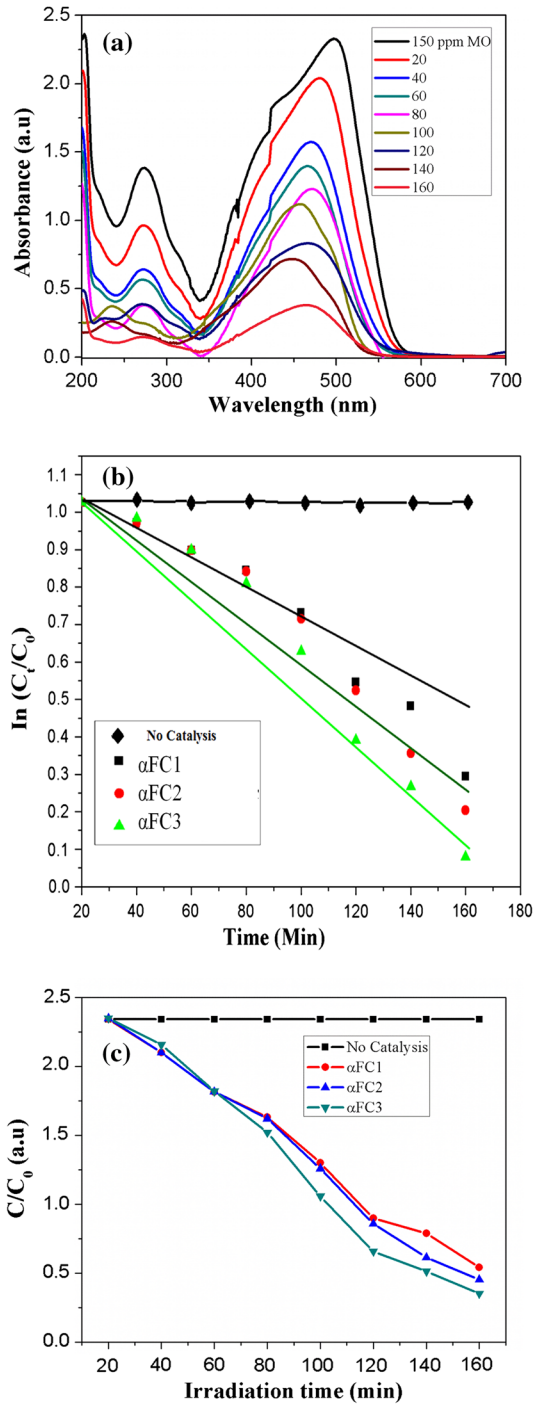
where  $A_t$  is the absorbance dyes with samples at any time  $t$  and  $C_0$  absorbance at initial time  $t=0$ . The pseudo-first-order kinetics rates of constant  $k$  are listed in Table 2. The kinetic constant has gradually increased corresponding to rise of the sample amount. The degradation efficiency of  $\alpha$ FC3 is high compared to  $\alpha$ FC1 and  $\alpha$ FC2. The reaction rate constant for  $\alpha$ FC3 is  $k=0.00651$  which is higher than 0.00349 and 0.00476, respectively, for  $\alpha$ FC1 and  $\alpha$ FC2. However,  $\alpha$ FC3 sample having low energy taken to degrade dyes of upconversion process was exhibited. So, the quantities of dyes ppm in the present work were very high as compared with other catalysts reported earlier [52]. The first-order kinetic constant plots of  $C_t/C_0$  versus time  $t$  are given in Fig. 10b. Degradation efficiency was calculated by applying the following equation [53].

$$\text{Degradation efficiency} = \frac{C_0 - C_t}{C_0} \times 100 \quad (4)$$

where  $C_0$  is the initial concentration of dye and  $C_t$  concentration at time  $t$ . The degradation ability of  $\alpha$ FC1,  $\alpha$ FC2, and  $\alpha$ FC3 is shown in Fig. 10c.  $\alpha$ FC3 sample was 100 mg and 150 ppm of MO dyes of 100 ml aqueous solution highly degraded in 2 h 40 min compared to other  $\alpha$ FC1 and  $\alpha$ FC2 samples. The combination of electron–hole pairs significantly increases the photocatalytic activities. The efficiency of  $\alpha$ FC1,  $\alpha$ FC2, and  $\alpha$ FC3 is 76%, 80%, and 85%, respectively. The photoinduced holes  $h^+$ , hydroxyl radicals  $\cdot OH$ , and superoxide radicals  $\cdot O_2^-$  are the main reactive species involved in the photodegradation process [54]. In the case of  $\alpha$ FC3, at pH 5 the superoxide radical and hole scavengers influence the photocatalytic process as shown in Fig. 11. These results suggest that under visible light irradiation, the nanocomposite materials and core–shell materials follow the similar photocatalytic degradation of MO [55, 56]. The core–shell structure leads to the fast separation of electrons and holes resulting in high photodegradation activity. The upconversion emission mainly stems from recombination of free charge carriers in the materials. The  $\alpha$ FC3 shows strong emission peak at 534 nm. The recombination rate of photoinduced electron–hole pairs greatly

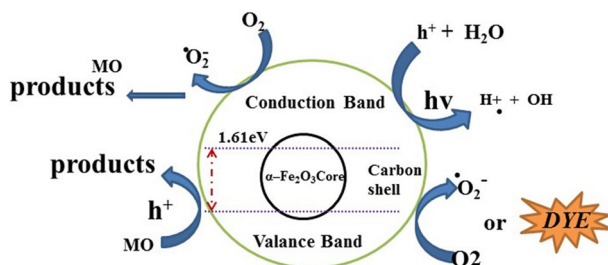


**Fig. 10** **a** Photodegradation of MO dye under UV-visible light irradiation. **b**  $\alpha\text{FC1}$ ,  $\alpha\text{FC2}$ , and  $\alpha\text{FC3}$  substances' photocatalytic degradation of pseudo-first-order kinetic spectra in the MO dyes. **c**  $\alpha\text{FC1}$ ,  $\alpha\text{FC2}$ , and  $\alpha\text{FC3}$  substance photocatalytic ability of degradation



**Table 2** The  $K_{app}$  values and photocatalytic efficiency (%) of  $\alpha$ FC1,  $\alpha$ FC2, and  $\alpha$ FC3

S. no	$K_{app}$ ( $\text{min}^{-1}$ )			Photocatalytic efficiency (%)		
	$\alpha$ FC1	$\alpha$ FC2	$\alpha$ FC3	$\alpha$ FC1	$\alpha$ FC2	$\alpha$ FC3
1	0.042571	0.042688	0.042682	76	80	85
2	0.018530	0.018548	0.019211			
3	0.009935	0.009944	0.009971			
4	0.006112	0.006034	0.005238			
5	0.002626	0.002296	0.000566			
6	0.00095	0.00128	0.00349			
7	0.00168	0.00349	0.00476			
8	0.00382	0.00495	0.00651			

**Fig. 11** Schematic photocatalytic mechanism of MO dyes for  $\alpha$ FC3 core-shell materials

suppressed which subsequently favors the enhancement of photocatalytic performance [57]. The high photocatalytic efficiency observed for  $\alpha$ - $\text{Fe}_2\text{O}_3$  sample is due to the synergistic effect between  $\alpha$ - $\text{Fe}_2\text{O}_3$  and carbon. The bandgaps of  $\alpha$ - $\text{Fe}_2\text{O}_3$  and  $\alpha$ FC3 are 2.2 eV and 1.61 eV, respectively [58]. The Coulomb interaction can reduce the energy of charge carrier changes. The increased carbon concentration enhances the light absorption ability which promotes the charge transfer and the formation of heterojunction. The fast interface charge transfer, and interfacial resistance of  $\alpha$ FC3, avoid massive recombination of ions and carbon layer on  $\alpha$ FC3 combinedly degrade the MO dyes [36].

### Trapping mechanism

The mechanism of photocatalytic activity of  $\alpha$ FC3 core-shell material has been hypothesized based on trapping percentage of active groups during photocatalytic reaction as shown in Fig. 12. The free radical scavengers are obtained from isopropanol (IPA) for  $\cdot\text{OH}$ , triethanolamine (TEOA) for  $\text{h}^+$ , and benzoquinone (BQ) for  $\text{O}_2^-$  [59]. The degradation efficiency of  $\alpha$ FC3 has

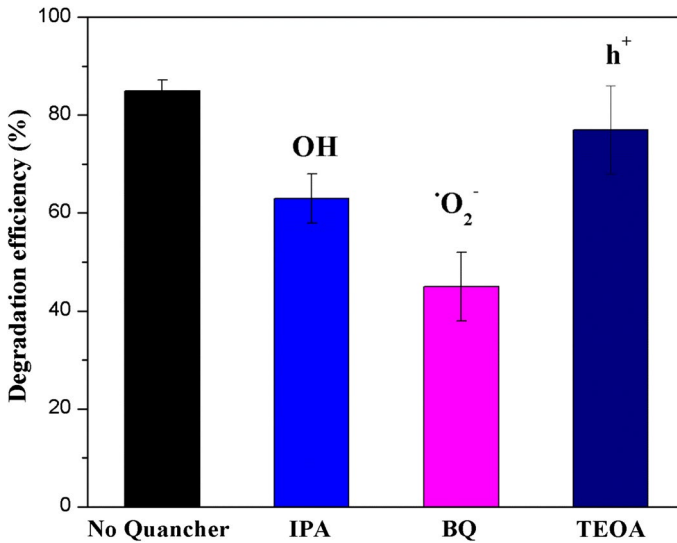
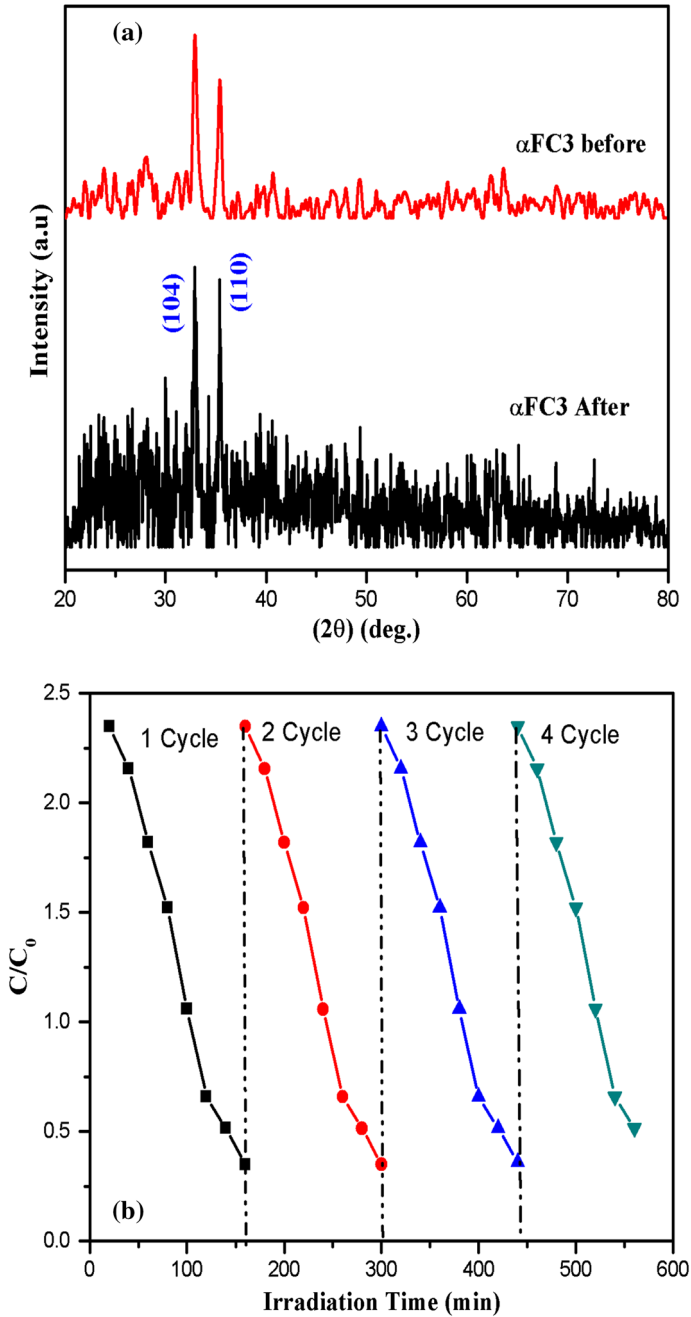


Fig. 12 Active species trapping in the photocatalytic reaction of  $\alpha\text{FC3}$  core-shell material

not affected for, e.g., 77% by the addition of 1 millimole isopropyl alcohol quencher. The TEOA was added to the reaction system 63% toward the trapped degradation. The degradation rate of MO is very high by choosing BQ to generate 42% of  $\text{O}_2^{\cdot-}$ . The luminescence study further confirms the high up-conversion rate that the recombination of electron and holes occurs by trapping  $\text{O}_2^{\cdot-}$  and  $\text{h}^+$  ions. In summary,  $\text{O}_2^{\cdot-}$  and  $\text{h}^+$  are the major reactive species during the photodegradation.

### Recyclability analysis

The stability and reusability were crucial evaluation basis in environmental governance. In Fig. 13a are shown the XRD spectra before and after four-cycle degradation of  $\alpha\text{FC3}$  sample. The Fig. 13b shows the four successive recycling experiments for the photocatalytic degradation of methyl orange dye. For each cycling experiments, the photocatalysts were collected, washed, centrifuged, dried, and reused with same condition. The photodegradation efficiency of  $\alpha\text{FC3}$  core-shell sample toward cycling still exceeded 84% after four cycles comparing to the first circulation (85%). The intensity of the peaks in the XRD pattern confirms the low crystallinity as shown in Fig. 13a. The above results indicated that the  $\alpha\text{FC3}$  core-shell sample was a stable and durable photocatalyst. Hence, the  $\alpha\text{FC3}$  core-shell sample had favorable stability and reusability during the photocatalytic degradation for high ppm in MO dyes.



**Fig. 13** **a** XRD spectra before and after four-cycle degradation of  $\alpha$ FC3 sample. **b** Cycling experiments for the photocatalytic degradation of  $\alpha$ FC3 sample under visible irradiation

## Conclusion

The  $\alpha$ FC1,  $\alpha$ FC2, and  $\alpha$ FC3 particles were successfully synthesized by hydrothermal method. Compared to  $\alpha$ FC1 and  $\alpha$ FC2, the  $\alpha$ FC3 showed a core–shell structure being single crystalline in nature. The upconversion luminescent efficiency was high for  $\alpha$ FC3 core–shell material with the contribution of Fe<sup>3+</sup> ions. The SEM morphology study indicated that Fe<sup>2+</sup> ions are the key factor for the formation of hematite core–shell structure. It is evident that nanoheterostructures are very important to their catalytic and fluorescence performance when it exposes at particular crystal planes and inclusion of active species. The degraded approach can be strongly depending on the upconversion luminescence of core–shell nanostructure. From Mott–Schottky plot of  $\alpha$ FC3, it is observed that the carrier density was increased by reduced flat-band potential. The photocatalytic stability of  $\alpha$ FC3 is high at 150 ppm in MO dyes. The increased carbon content in  $\alpha$ FC3 raises the oxidation number of the sample. The photocurrent study indicated that the electron density has been improved and stable after four cycles. This type of core–shell has distinct textural properties employing effectively in MO dye degradation of industrial wastewater pollution.

**Acknowledgements** The author M. Gnanasekaran thanks to Department of Nanoscience and Nanotechnology, Karunya University, and Sophisticated Test and Instrumentation Centre, Kochi University, Kochi, 682 022, Kerala, India, for the support of analytical measurements.

**Author contributions** All the authors contributed to the discussion and preparation part of the manuscript. The final version of the manuscript was approved by all authors.

## Compliance with ethical standards

**Conflict of interest** The authors declare that they have no conflict of interest.

## References

1. S.H.S. Chan, T. Yeong Wu, J.C. Juan, C.Y. Teh, J. Chem. Technol. Biotechnol. **9**, 1130 (2011)
2. A.S. Stasinakis, Glob. Nest J. **3**, 376 (2008)
3. K. Kestioğlu, T. Yonar, N. Azbar, Process Biochem. **7**, 2409 (2005)
4. E.J. Hart, A. Henglein, J. Phys. Chem. **20**, 4342 (1985)
5. A.E. Alegria, Y. Lion, T. Kondo, P. Riesz, J. Phys. Chem. **12**, 4908 (1989)
6. S. Bhukal, M. Dhiman, S. Bansal, M.K. Tripathi, S. Singhal, RSC Adv. **2**, 1360 (2016)
7. X. Huang, X. Zhan, C. Wen, F. Xu, L. Luo, J. Mater. Sci. Technol. **5**, 855 (2018)
8. H. Guo, M. Chen, Q. Zhong, Y. Wang, W. Ma, J. Ding, J CO2 Util **33**, 233 (2019)
9. S. Balu, S. Velmurugan, S. Palanisamy, S.W. Chen, V. Velusamy, T.C. Yang, E.S.I. El-Shafey, J. Taiwan Inst. Chem. Eng. **99**, 258 (2019)
10. Z. Li, C. Li, Y. Mei, L. Wang, G. Du, Y. Xiong, Nanoscale **7**, 3030 (2013)
11. D.X. Xu, Z.W. Lian, M.L. Fu, B.L. Yuan, J.W. Shi, H.J. Cui, Appl. Catal. B Environ. **142**, 377 (2013)
12. W. Wang, M.Y. Ding, C.H. Lu, Y.R. Ni, Z.Z. Xu, Appl. Catal. B Environ. **144**, 379 (2014)
13. X. An, C.Y. Jimmy, RSC Adv. **8**, 1426 (2011)
14. F. Auzel, C. R. Acad. Sci. B **262**, 1016 (1966)
15. F. Auzel, Chem. Rev. **104**, 139 (2004)
16. H. Yin, Y. Zhao, Q. Hua, J. Zhang, Y. Zhang, X. Xu, Y. Long, J. Tang, F. Wang, Front Chem. **7**, 58 (2019)
17. A. Kusior, M. Synowiec, K. Zakrzewska, M. Radecka, Crystals **9**, 163 (2019)

18. H. Wang, J. Mao, Z. Zhang, Q. Zhang, L. Zhang, P. Li, *Toxins* **11**, 105 (2019)
19. T. Wang, M. Sun, H. Sun, J. Shang, P.K. Wong, *Appl. Surf. Sci.* **464**, 43 (2019)
20. S. Balu, K. Uma, G.T. Pan, T. Yang, S. Ramaraj, *Materials* **11**, 1030 (2018)
21. X. Peng, M.C. Schlamp, A.V. Kadavanich, A.P. Alivisatos, *J. Am. Chem. Soc.* **30**, 7019 (1997)
22. J. van Embden, J. Jasieniak, D.E. Gómez, P. Mulvaney, M. Giersig, *Aust. J. Chem.* **7**, 457 (2007)
23. P.M. Forster, P.M. Thomas, A.K. Cheetham, *Chem. Mater.* **14**, 17 (2002)
24. J.H. Bang, K.S. Suslick, *Adv. Mater.* **10**, 1039 (2010)
25. G. Munusamy, K. Varadarajan, S. Narasimhan, U.G. Thangapandiyam, *Res Chem Intermed.* **12**, 7815 (2018)
26. X. Zhu, Q. Su, W. Feng, F. Li, *Chem. Soc. Rev.* **4**, 1025 (2017)
27. L. Vayssieres, C. Sathe, S.M. Butorin, D.K. Shuh, J. Nordgren, J. Guo, *Adv. Mater.* **19**, 2320 (2005)
28. X. Sun, Y. Li, *Angew. Chem.* **5**, 607 (2004)
29. D. Andreeva, T. Tabakova, V. Idakiev, P. Christov, R. Giovanoli, *Appl. Catal.* **1**, 9 (1998)
30. M. Li, H. He, *Vacuum* **143**, 371 (2017)
31. A. Umar, R. Ahmad, A. Al-Hajry, S.H. Kim, M.E. Abaker, Y.B. Hahn, *New J. Chem.* **12**, 5873 (2014)
32. J. Yang, F. Zhang, H. Lu, X. Hong, H. Jiang, Y. Wu, Y. Li, *Angew. Chem.* **37**, 11039 (2015)
33. A.K. Patra, S.K. Kundu, A. Bhaumik, D. Kim, *Nanoscale* **1**, 365 (2016)
34. C.J. Weng, Y.L. Chen, C.M. Chien, S.C. Hsu, Y.S. Jhuo, J.M. Yeh, C.F. Dai, *Electrochim. Acta* **95**, 162 (2013)
35. W. Cai, J. Yu, B. Cheng, B.L. Su, M. Jaroniec, *J. Phys. Chem. C* **33**, 14739 (2009)
36. Y.H. Sun, S. Liu, F.C. Zhou, J.M. Nan, *Appl. Surf. Sci.* **390**, 175 (2016)
37. D. Qi, H. Zhang, J. Tang, C. Deng, X. Zhang, *J. Phys. Chem. C* **20**, 9221 (2010)
38. K. Cheng, Y.M. Zhou, Z.Y. Sun, H.B. Hu, H. Zhong, X.K. Kong, Q.W. Chen, *Dalton Trans.* **19**, 5854 (2012)
39. F. Zhang, H. Hu, H. Zhong, N. Yan, Q. Chen, *Dalton Trans.* **16**, 6041 (2014)
40. C.A. Gorski, M.M. Scherer, *Aquat. Redox Chem.* **1071**, 315 (2011)
41. Y.P. He, Y.M. Miao, C.R. Li, S.Q. Wang, L. Cao, S.S. Xie, G.Z. Yang, B.S. Zou, C. Burda, *Phys. Rev. B.* **12**, 125411 (2005)
42. P. Kubelka, *Josa* **5**, 448 (1948)
43. G.H. Wang, W.C. Li, K.M. Jia, B. Spliethoff, F. Schüth, A.H. Lu, *Appl. Catal. A Gen.* **1–2**, 42 (2009)
44. N. Bloembergen, *Phys. Rev. Lett.* **3**, 84 (1959)
45. J.L. Clark, P.F. Miller, G. Rumbles, *J. Phys. Chem. A* **24**, 4428 (1998)
46. A. Salinas-Castillo, M. Ariza-Avidad, C. Pritz, M. Campubí-Robles, B. Fernández, M.J. Ruedas-Rama, A. Megia-Fernández, A. Lapresta-Fernández, F. Santoyo-Gonzalez, A. Schrott-Fischer, L.F. Capitan-Vallvey, *Chem. Commun.* **11**, 1103 (2013)
47. X. Wang, L. Cao, S.T. Yang, F. Lu, M.J. Meziani, L. Tian, K.W. Sun, M.A. Bloodgood, Y.P. Sun, *Angew. Chem. Int. Ed.* **31**, 5310 (2010)
48. D.A. Wheeler, G. Wang, Y. Ling, Y. Li, J.Z. Zhang, *Energ Environ. Sci.* **5**, 6682 (2012)
49. G.C.N.N.A.R. Schön, J. Tummavuori, B. Lindström, C.R. Enzell, C.G. Swahn, *Acta Chem. Scand.* **27**, 2623 (1973)
50. S. Shen, J. Zhou, C.L. Dong, Y. Hu, E.N. Tseng, P. Guo, L. Guo, S.S. Mao, *Sci. Rep.* **4**, 6627 (2014)
51. Y. Chen, J. Peng, H. Xiao, H. Peng, L. Bu, Z. Pan, Y. He, F. Chen, X. Wang, S. Li, *Appl. Surf. Sci.* **420**, 773 (2017)
52. L. Jiang, X. Yuan, G. Zeng, X. Chen, Z. Wu, J. Liang, J. Zhang, H. Wang, H. Wang, *ACS Sustain. Chem. Eng.* **7**, 5831 (2017)
53. J. Liao, S. Lin, L. Zhang, N. Pan, X. Cao, J. Li, *ACS Appl. Mater. Interfaces.* **1**, 171 (2011)
54. S. Min, G. Lu, *J. Phys. Chem. C* **37**, 19644 (2012)
55. Y. He, L. Zhang, M. Fan, X. Wang, M.L. Walbridge, Q. Nong, Y. Wu, L. Zhao, *Sol. Energy Mater. Sol. Cells* **137**, 175 (2015)
56. J. Zhang, X. Liu, L. Wang, T. Yang, X. Guo, S. Wu, S. Wang, S. Zhang, *Nanotechnology* **18**, 185501 (2011)
57. C. Zhao, G. Tan, W. Yang, C. Xu, T. Liu, Y. Su, H. Ren, A. Xia, *Sci. Rep.* **6**, 38603 (2016)
58. H. Fu, S. Sun, X. Yang, W. Li, X. An, H. Zhang, Y. Dong, X. Jiang, A. Yu, *Powder Technol.* **328**, 389 (2018)
59. L. Ye, X. Liu, Q. Zhao, H. Xie, L. Zan, *J. Mater. Chem. A* **31**, 8978 (2013)

**Publisher's Note** Springer Nature remains neutral with regard to jurisdictional claims in published maps and institutional affiliations.